

Design and aerodynamic analysis of a VTOL tilt-wing UAV

Hasan ÇAKIR*, Dilek Funda KURTULUŞ

Aerospace Engineering Department, Graduate School of Natural and Applied Sciences,
Middle East Technical University, Ankara,

Received: 08.05.2021

Accepted/Published Online: 21.10.2021

Final Version: 21.03.2022

Abstract: The aerodynamic design and analysis of an Unmanned Air Vehicle, capable of vertical take-off and landing by employing fixed four rotors on the tilt-wing and two rotors on the tilt-tail, will be presented in this study. Both main wing and the horizontal tail can be tilted 90°. During VTOL, transition and forward flight, aerodynamic and thrust forces have been employed. Different flight conditions, including the effects of angle of attack, side slip, wing tilt angle and control surfaces deflection angle changes, have been studied with CFD analysis. For a Tilt-Wing UAV, there are challenges like high non-linearity, vulnerability to disturbances during hover and transition, cross-coupling between three axes, very low time to double amplitude of the open-loop system. Therefore, the aerodynamic analysis has been done in detail considering especially the challenges in transition phase of the flight envelope.

Key words: Vertical Takeoff and Landing (VTOL); Tilt-Wing, Unmanned Air Vehicle (UAV)

1. Introduction

In terms of wing motion, unmanned air vehicles can be divided into three categories. Fixed-wing, rotary-wing, and flapping-wing aircraft are the three types [1]. Each of the three types has advantages and disadvantages in comparison to the others. Although fixed-wing airplanes have a disadvantage in terms of take-off and landing distances, rotary-wing and flapping-wing airplanes have issues with payload ability and long-range flight as compared to fixed-wing airplanes. Combining the benefits of all three types of UAVs to reveal a more effective UAV design is generally the main goal. As aviation technology advances, the obstacles that must be overcome become more complex. In recent years, researchers around the world have begun to investigate the development of a reliable controller for VTOL systems in the transition phase of flight [2]. However, there are few examples because there is no consistent way to construct an ideal controller capable of conducting vertical, transitional, and horizontal flights at the same time. The transition between flight modes is both a complicated and exciting problem to solve. Fixed-wing UAVs are the most popular platforms for long endurance and range, with researchers reporting that a mini fixed-wing UAV has at least two times the flight endurance of a mini helicopter [3]. Rotary-wing and flapping-wing UAVs, such as helicopters, multi-rotors, and flapping-wing micro air vehicles (FWMAVs), on the other hand, can hover, but their high-power requirements restrict their flight time and range [3]. Due to their technical complexity, helicopters are difficult and costly to run, and they need frequent maintenance. Multi-rotors have a basic mechanical design, but their payload capacity is limited due to their high-power requirements. Despite being mechanically simpler platforms, tail-sitters are difficult to control and more vulnerable to disturbances [3]. While tilt-rotors have a decent endurance, they lose a lot of thrust in

*Correspondence: e204293@metu.edu.tr

vertical flight because the rotors are vertical to the wing.

VTOL-capable UAVs have recently piqued the interest of both the scientific community and industry. The method of integrating VTOL and fixed-wing control elements distinguishes these platforms in their configurations. According to scientific research on VTOL capable platforms, NASA GL-10[4] is about 30 kg in weight and has a flight endurance of 2 hours. It has a service ceiling of around 5000 feet and flies at 15 to 30 m/s. It is equipped with ten motors, eight on the main wing and two on the tail. The QTW-UAV [5], is a four-motored drone with a take-off weight of 24 kg. In VTOL mode, the wings produce lift when they are tilted due to the accelerated air generated by the rotor blades. This function gives them an extra control input when maneuvering the plane in VTOL and transition modes. The AVIGLE [6], has a take-off weight of 10 kg and is capable of conducting missions at speeds ranging from 0 to 40 m/s. This aircraft is built with two rotors, which is distinct from the other examples. Carbon fiber is used to make it. A small fan blade is used to stabilize the moment; thus, we can assume that this UAV has three rotors in all. This form is considered riskier than the others because if a rotor fails, the aircraft would become uncontrollable. The QUX-02A [7] has two wings and four rotors, a take-off weight of 4.2 kg, and can perform missions at speeds of 10 to 25 m/s. For the Smart UAV development program, Korea Aerospace Research Institute developed and produced a Tilt-Rotor Aircraft [8]. They designed a scaled model and successfully tested it for the sake of the program. The aircraft's overall take-off weight is about 210 kg, and its maximum speed is 250 km/h. It can fly for 5-6 hours and has a wingspan of around 5 meters.

SUAVI ([9] and [10]) has a cruise speed of 17 m/s and is specifically designed for surveillance. In the study, the designer has avoided from the complexity as much as possible while designing the controller and they have mainly concentrated on the controller. The aircraft is made of carbon fiber and has four rotors and a take-off weight of 4.5 kg. Since it uses two tandem wings that are similar and positioned sequentially, it has symmetry in the pitch axis. This symmetry allows for a simpler flight controller configuration. However, since the backward wing is influenced by the front wing's down-wash, the aerodynamic performance suffers. Onen et al. [11] realized hover for a tri-copter fixed-wing UAV configuration in another report. The method of transition used in switching the aircraft between flight modes is the key difference in these experimental VTOL platform studies. By stalling the aircraft in transition, a tail-sitter platform tilts the fuselage by control surfaces [3]. In transition maneuvers, a tilt-rotor tilts the fuselage by adjusting the angular positions of its rotors and operating the wings in stall conditions. The fuselage of a tilt-wing aircraft is parallel to the ground and the wings are tilted and fly at high angles of attack. TURAÇ [12], with its flying wing-tiltrotor and ducted fan configuration, is another fascinating example. It has a 4.2 m wing span and a cruise speed of 25 m/s. The TURAÇ has a maximum take-off weight of 47 kg and a payload of 8 kg. ZANKA-IV ([13]) has both fixed-wing and helicopter flight mode with passive and active morphing mechanisms. A new autonomously controlled tilt-duct vertical takeoff and landing uninhabited aerial vehicle concept is proposed by [14].

The aim of these studies was to build an aircraft with a simpler flight controller than previous designs, albeit at the cost of aerodynamic efficiency. Since it has less control complexity, most experiments on the tilt-wing aircraft concept use motors that are symmetrically positioned along the pitching and rolling axes. However, since they use a tandem wing instead of a pair of wings and a horizontal tail, these types do not have very good aerodynamic performance. Since the NASA GL-10 has a wing and horizontal tail pair, its controller is a little more complicated, but it is aerodynamically sound. The aim of the current research is to find a VTOL UAV platform that has adequate aerodynamic performance, as well. The controller performance of the air vehicle will be presented in future studies. The proposed device will be electric-powered and radio-controlled,

with a 60-minute flight time, a one-kilometer operating range, a 2.5-kg payload size, and a cruise speed of 15-25 m/s. The VTOL UAV, which will practice take-off and landing using thrust supplied by electric motors installed in front of a tilting wing that is vertical to the XY plane of the body, will perform level flight after take-off by having the wings parallel to the body. A commercial CFD code (FLUENT [15]) was used to obtain the stability coefficients that will be required when designing the controller.

2. Design Methodology/Approach

The transition time between vertical and forward flight is the most difficult part of tilt-wing aircraft design. This study's main goal is to generate enough aerodynamic force to lift the aircraft in the shortest time possible as the aircraft's velocity increases. In order to maximize the use of aerodynamic forces rather than thrust forces during conversion flight, the stall speed should be kept as low as possible. By looking for similar platforms in the literature, the target payload capacity was calculated to be 2.5 kg. The total weight is estimated to be about 10 kg using the empty weight calculation formulas given in [16]. The structural sections of the aircraft were estimated to weigh about 2 kg using the CAD model. Our target design weight is 9.5 kg after selecting the motor. The airfoil is chosen after the target weight of 9.5 kg has been calculated. Since the maximum Reynolds Number is calculated to be about 500,000 and the flight velocity isn't too high, it's normal to choose an airfoil with a high L/D ratio. However, a high maximum lift coefficient will be needed when transitioning from transition between flight modes to level flight, which is the most challenging part of the flight. As a consequence, in addition to the L/D ratio, the maximum lift coefficient is also a factor in the airfoil selection process. Using the XF5R5 [17] program, different airfoils were analyzed at different Reynolds Numbers. For the target Reynolds number interval, the most suitable airfoil that meets the requirements is S1223 in the airfoil family. Because of its high lift coefficient at stall speed, the S1223 airfoil was chosen. Low drag and a high L/D ratio usually take precedence, but in this case, we want to keep the stall speed as low as possible to avoid the transition process. Typical taper ratio has been chosen for the design. Considering manufacturability, trailing edge sweep angle has been chosen as zero. Choosing the taper ratio and trailing edge sweep angle values has resulted in the leading edge sweep angle to be five degrees. According to [16], the fuselage length for comparable aircrafts should be about 2 meters as a starting point. However, after performing a longitudinal stability study, it was determined that a fuselage length of 1.8 meters would have adequate pitch control strength. Using the [16] relation, the fuselage equivalent diameter was determined to be 0.2 m. A trade analysis was conducted to determine the impact of changes in aspect ratio, wing span, and wing area on the L/D ratio (Figure 1)). The ideal wing configuration reduces drag while maintaining lift-off efficiency. Increased wing area reduces stall speed while increasing total drag by increasing aircraft dimensions and structural weight, according to our research. Increasing the aspect ratio reduces stall speed while also increasing the structural weight of the wing, which is fatal for the tilting spars. Because of the tilting spar's structural failures, a restriction on wingspan is used. The aspect ratio is restricted to a range of 5 to 7, which is common for fixed-wing aircraft. Due to the wingspan constraint, the highest scoring wing configuration has an aspect ratio of 6.95 and a wing area of 0.575 m². There are four key choices for the horizontal stabilizer: thin or thick airfoils, symmetric or semi-symmetric airfoils. The drag and lift characteristics of an airfoil are determined by its thickness. A thicker airfoil may produce more lift, but it may also produce more drag. Since the stabilizer's sole objective is to provide moment, a thin airfoil with low drag was chosen, and the limited lift force was compensated for by designing a slightly longer arm. Symmetric airfoils are widely used in UAVs, gliders, and light aircraft because they provide the vehicle with more stability and the same pitch moment for both positive and negative AoA. A semi-symmetric airfoil,

on the other hand, could potentially obtain a marginally higher overall lift coefficient for the entire aircraft, allowing for a higher pitch-up moment. It was decided to use the symmetrical NACA 0009 airfoil because it adds sufficient stability and the potential lift addition from the horizontal stabilizer would be negligible due to its limited surface area in comparison to the main wing surface area. To balance the high lift provided by the wing, the horizontal tail volume coefficient is set to 0.61. The new study’s design specification is tabulated in Table 1, and the design is depicted in Figure 2.

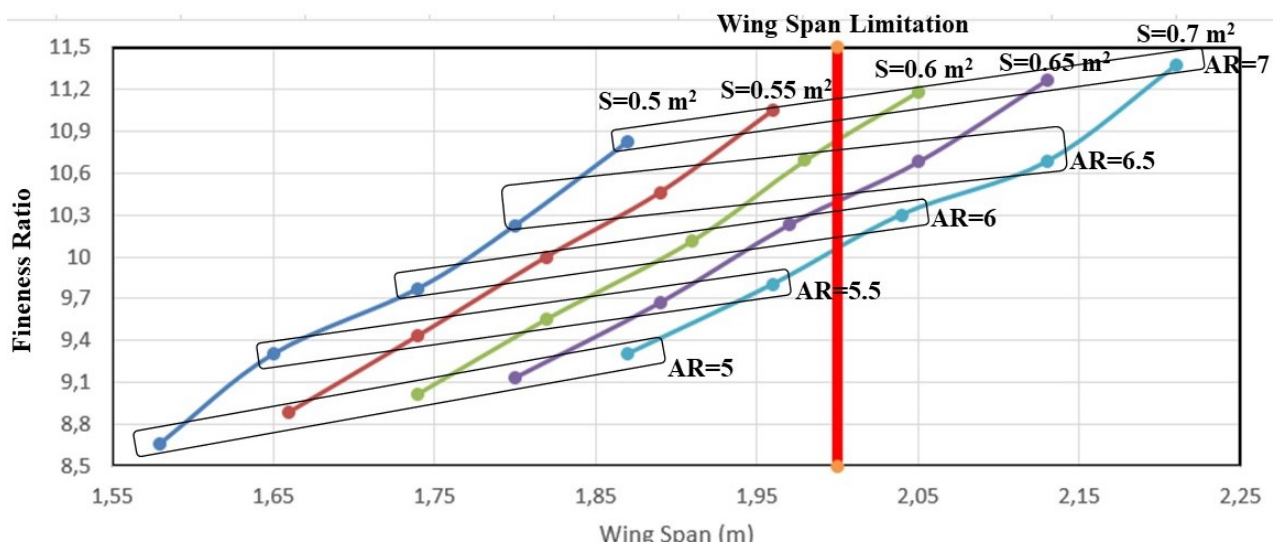


Figure 1. Trade study on wing geometrical parameters.

Table 1. Aircraft Specifications.

Term	Value	Term	Value	Horizontal Tail	Value
Length	1.8 m	Wingspan	2 m	Airfoil Type	NACA 0009
Weight	9.5 kg	Wing Area	0.575 m ²	Root Chord	0.2 m
Speed	0-25 m/s	MAC	0.33 m	Sweep Angle	5°
Propulsion Type	Electric Driven	Root Chord	0.36 m	Taper Ratio	0.8
Engine Number	Six	Airfoil Type	S1223		
		Taper Ratio	0.7		
		Aspect Ratio	6.95		
		Sweep Angle	5°		

The inertia and center of gravity of the wing will change as it rotates around the fuselage. To prevent the aircraft’s CG from changing, the wing’s CG is located at the center of the tilting line, which matches up with the middle of the wing spar (Figure 3). The tail is subject to the same condition. The adjustment in aircraft CG and inertia matrix during the transition would be zero if this approach is used.

2.1. Propulsion System Selection

Power loading, or the instantaneous power output of the propulsion package divided by the total weight of the aircraft, is a common way to describe model aircraft flight efficiency. To be capable of vertical flight, electric-

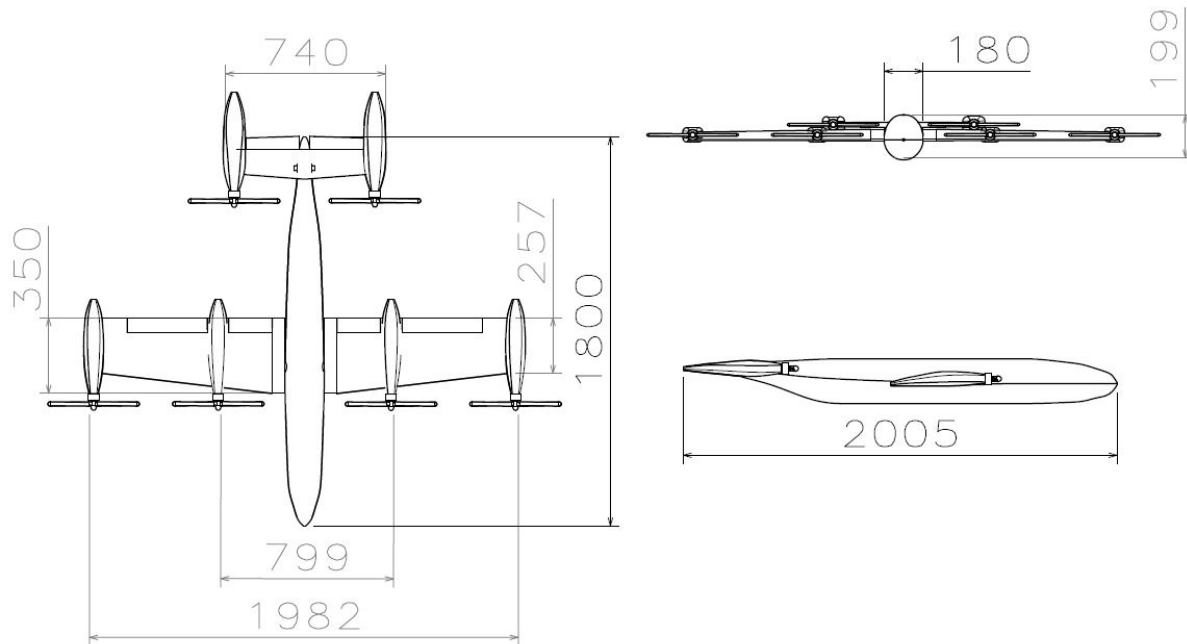


Figure 2. The overall dimensions of the aircraft.

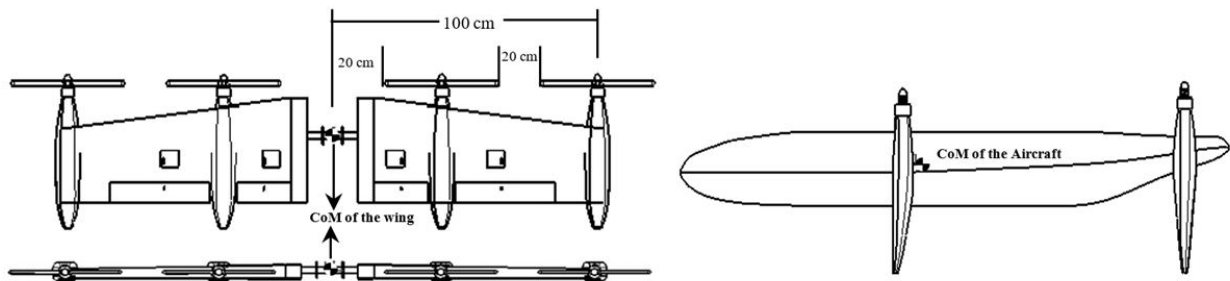


Figure 3. Center of gravity of tilting wing and the aircraft.

powered UAVs must have a power loading of more than 300 W/kg [18]. Until further trade studies could completely optimize the propulsion kit, 300 W/kg was used as an initial assumption based on prior experience with Li-Po batteries. The literature survey [18] and other model airplanes were used to make additional weight assumptions for the propulsion system. Specifically, the propulsion system would weigh 40 % of the total aircraft weight (3.6 kg) and the battery pack would weigh 50 % of the propulsion kit weight (1.8 kg). [19], introduces the distributed electric propulsion model, which shows that increasing the number of propellers increases the power to weight ratio. During even hover conditions, this phenomenon provides airflow that flows all over the wing and tail. This condition allows us to fly the aircraft with more aerodynamic efficiency. To have enough propeller slipstream on the wing during the hover and transition process, a propeller that covers the entire wing and tail was chosen (Figure 3)). Since the propulsion system provides sufficient power to stabilize the aircraft in the yaw

axis during transition and forward flight, no vertical stabilizer is needed. The propulsion system was chosen to increase the aircraft’s endurance and range while reducing its weight. The motor, battery, and propeller pairs were accurately determined using the Neu-Motors e-Calc motor and battery kit selection tool [20]. The total weight of the aircraft, the number of engines, the wing area, drag coefficient, cross-sectional area, engine type, battery, driver, and propeller are all inputs into this instrument. The airframe weight was determined to be 2 kg, the target payload was 2.5 kg, and electronic components were estimated to weigh around 1 kg. As a result, the total aircraft weight is assumed to be 5.5 kg, except the motor, battery, and propeller. Since the intention is to cover the wing with propeller slipstream, the propeller’s diameter should be about 15 inches to cover a fair area. It was decided to use the motor pairs mentioned in Table 2 as a result of the iterative selection process. Forward and rear motors produce different amounts of thrust. The forward motors are the main thrust generators, while the rear motors are used for moment balancing. Only forward motors will be used during forward flight since the horizontal stabilizer will be active to offset the pitch moment. If more endurance is desired, the rear motors can also be used in forward flight.

Table 2. Motor specifications.

Term	Forward Motors	Rear Motors
Motor	NeuMotors 1112/6D(1092)	NeuMotors 1902/4Y(1000)
Controller	CC Phoenix Edge 130	CC Phoenix Edge 75
Battery Cell	LiPo 450 mAh-20/30C 6X24	LiPo 1200 mAh-20/30C 3X4
Propeller	APC Electric E 14X16	APC Electric E 8X10
Weight (Each Pack)	748 grams	460 grams
Shaft Power	363.9 W	122.6 W

3. Aerodynamic Analysis

The vehicle body-fixed frame, F_B , as its origin B located at the instantaneous CG of the air vehicle, as shown in Figure 4. Aerodynamic forces are generated as a vehicle travels through the air and encounters a relative wind over its body.

The propeller slipstream will provide additional airspeed for VTOL and Transition mode. In forward motion, the propeller slipstream velocity is assumed to be negligible. For similar flight phases, this additional airspeed should be added to the overall airspeed. We may add it to the propulsion coordinates (wing coordinates) as given below, since the additional speed would only be in the opposite direction of the engine.

$$\{\vec{v}_{B/W}^E\}^{(P(F))} = \begin{bmatrix} -V_{Prop} \\ 0 \\ 0 \end{bmatrix} \tag{1}$$

The components of the aerodynamic force in the perpendicular and parallel to flow directions, respectively, are known as lift and drag. As a consequence, in the wind coordinate system, lift (L), drag (D), and crosswind force (C) are all directly measured. Using body-axes components of the aerodynamic force vector $\{\vec{f}_a\}^{(B)} = [\vec{f}_{aXB} \ \vec{f}_{aYB} \ \vec{f}_{aZB}]^T$, together with the transformation matrix $\check{T}^{(B,W)}$ of wind with respect to vehicle body coordinates, yields the wind-axes components of the aerodynamic force vector

conversely,

$$\{\vec{f}_a\}^{(B)} = \check{T}^{(B,W)} \{\vec{f}_a\}^{(W)} = [\check{T}^{(W,B)}]^T \{\vec{f}_a\}^{(W)} \quad (8)$$

$$\begin{bmatrix} C_X \\ C_Y \\ C_Z \end{bmatrix} = \begin{bmatrix} c_{(\beta)}c_{(\alpha)} & -s_{(\beta)}c_{(\alpha)} & -s_{(\alpha)} \\ s_{(\beta)} & c_{(\beta)} & 0 \\ c_{(\beta)}s_{(\alpha)} & -s_{(\beta)}s_{(\alpha)} & c_{(\alpha)} \end{bmatrix} \begin{bmatrix} -C_D \\ -C_C \\ -C_L \end{bmatrix} \quad (9)$$

giving;

$$\begin{aligned} C_X &= -c_{(\alpha)}c_{(\beta)}C_D + c_{(\alpha)}s_{(\beta)}C_C + s_{(\alpha)}C_L \\ C_Y &= -s_{(\beta)}C_D - c_{(\beta)}C_C \\ C_Z &= -s_{(\alpha)}c_{(\beta)}C_D + s_{(\alpha)}s_{(\beta)}C_C - c_{(\alpha)}C_L \end{aligned} \quad (10)$$

The velocity of the propeller slipstream is calculated using (11) which is given in [21]. The equation assumes that as propeller thrust increases, so does induced velocity through the propeller disk.

$$V_{prop} = \sqrt{\frac{T}{2\rho A}} \quad (11)$$

where T is thrust, ρ is air density and A is the propeller disc area, respectively. Propeller velocity dominates the body velocity vector for the tilt-angles between 90° to 45° , while the opposite is true for the angles between 45° and 0° . It should be remembered that for all flight conditions, effective velocity is calculated using the wing AoA. Effective velocity changes during the transition phase has been shown in Figure 5.

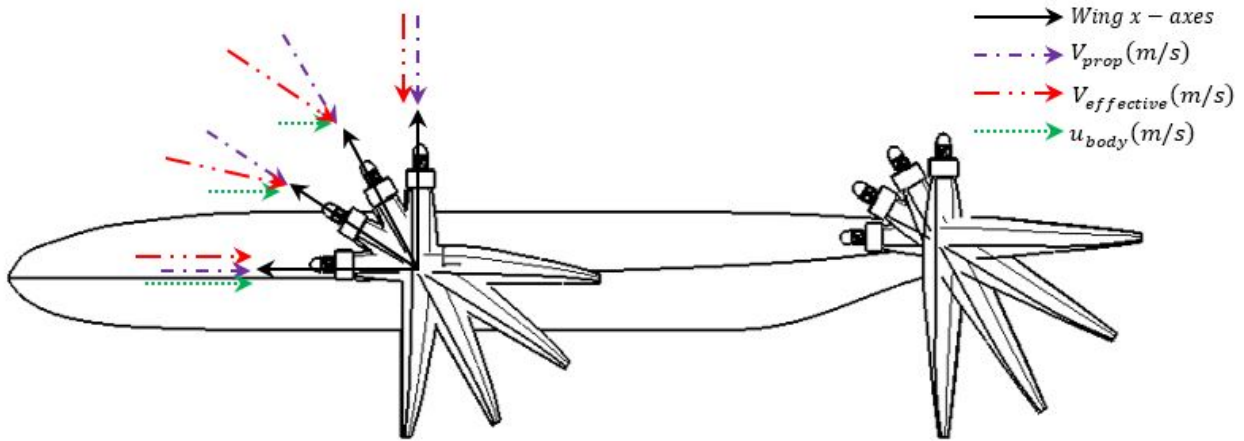


Figure 5. Effective velocity changes during the transition

4. Results and Discussion

ANSYS/Fluent was used to construct the aerodynamic database. The CFD data was generated using 63 CAD geometries (a combination of seven tilt angle positions, three elevator deflections, and three aileron deflections). When the airspeed is set to 20 m/s, CFD results are obtained. The density and viscosity of the air are assumed to

remain constant. During the flight, the reference length does not change. The only variable in the aerodynamic analysis is airspeed, which covers the entire flight envelope. The Reynolds number for level flight has been calculated to be 500000, while the Reynolds number for vertical flight has been calculated to be 250000. For this study, Reynolds number and airspeed can be assumed to be constant. Additional analyses for variable airspeed showed that assuming constant airspeed for all flight conditions resulted in just a 3% error in lift coefficient and a 2.5% error in drag coefficient, which is acceptable. A grid refinement study was conducted to determine the optimal grid number, which, by decreasing the grid number, provides an effective solution. For this analysis, a mesh size of four million is appropriate. The results of a grid refinement study showed that after four million elements, the results were constant (Figure 6), implying that between four and five million elements would suffice for this research. The convergence characteristics of the drag and lift coefficients were the same. The grid refinement analysis was carried out using the CAD geometry that had been prepared for $\delta_{TW} = 0^\circ, \delta_a = 0^\circ, \delta_e = 0^\circ$.

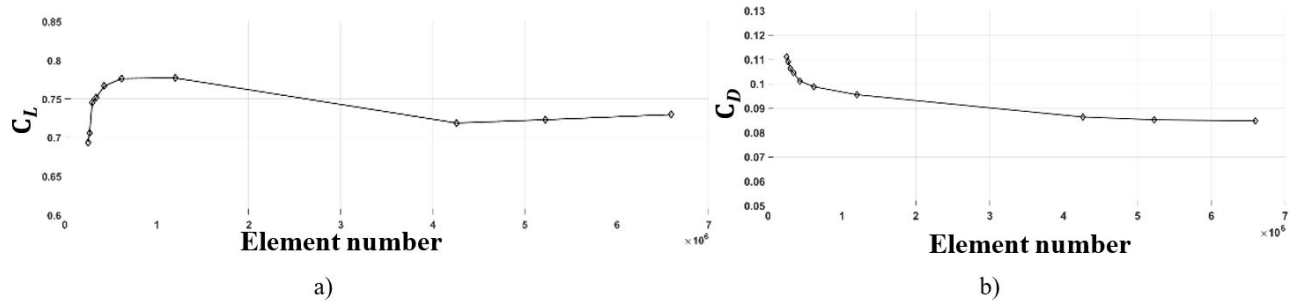


Figure 6. Grid refinement study for C_L and C_D

There were 5670 runs completed during the CFD analysis phase. The Spalart Allmaras Turbulence model (1 Eq.) was chosen because it is suitable for low Reynolds number applications. The thickness of the first layer of the boundary layer was calculated using a standard y^+ value, which is one for Spalart Allmaras Turbulence Model. The thickness of the first layer of the boundary layer has been determined to be 0.03 mm. According to the grid refinement report, element size was determined to be between 4 and 5 million. Due to the 63 different CAD geometries, there may be minor variations in element dimension. Since the flight level is expected to be near to sea level, the air pressure is assumed to be 101325 Pa. During the transition, the propeller slipstream produces an additional airspeed of 7-10 m/s on the wings ([22]). Moreover, during the transition between flight modes, the body velocity increases from 0 to 16.1 m/s. During the entire flight envelope, overall airspeed over the aircraft varies between 10 and 20 m/s. As a result, airspeed is assumed to be 20 m/s under all flight conditions. Additional analyses for variable airspeed showed that assuming constant airspeed for all flight conditions resulted in just a 3% error in lift coefficient and a 2.5% error in drag coefficient. Figure 7, which depicts the zero-tilt angle, aileron, and elevator deflection geometry, is an example of the grid domain. In front of the aircraft, the grid domain has a hemisphere with a radius of 25 meters and a cylinder with a length of 50 meters. Unstructured triangular grids have been employed for the CFD models.

The variance in lift coefficient for the entire aircraft indicates that there will be no major C_L adjustment in conversion mode; the maximum lift coefficient has been observed in forward flight conditions, as predicted (Figure 8). The CFD analysis is performed in wing coordinates, which means that a zero AoA indicates that the wing and airspeed are in the same line. Tilt-Wing effect on C_L has been shown at zero AoA in Figure 8.b.

The minimum drag coefficient has been determined to be at zero AoA for all tilt-wing angles (Figure 9). As the tilt angle is decreased, the drag coefficient drops significantly. The control allocation will be affected directly by changes in the drag coefficient.

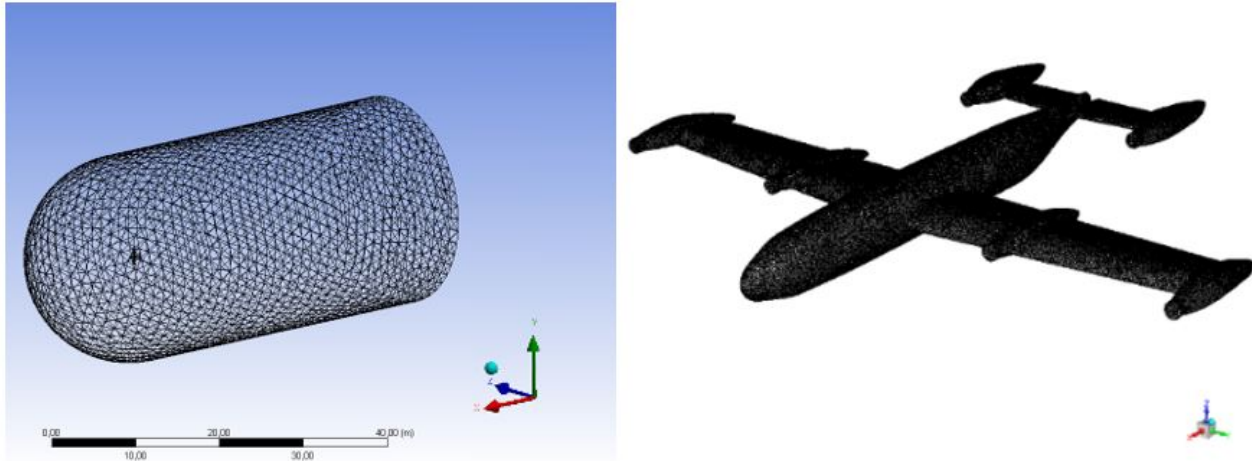


Figure 7. Grid domain of the study.

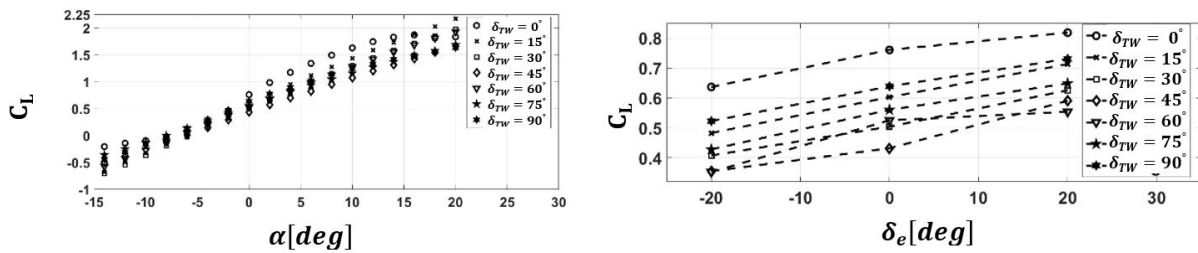


Figure 8. Lift coefficient, C_L , variation with angle of attack for different tilt- wing angles

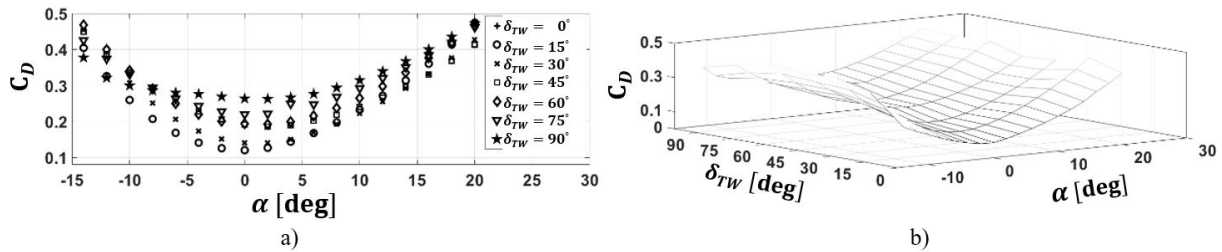


Figure 9. Drag coefficient, C_D , variation with angle of attack for different tilt- wing angles.

The C_m difference in relation to the Center of Gravity provides us with information about the aircraft's longitudinal axis stability (Figure 10). Except for vertical flight, our aircraft is statically stable in any tilt angle. By increasing the elevator deflection, we were able to achieve an acceptable rise in pitch moment. The aircraft's

pitch non-linearity and pitch up behavior are permissible. Figure 10.b shows the pitching moment variation with AoA for different elevator deflections when tilt-wing angle is zero.

The roll moment variation with respect to AoA for $\delta_a = 20^\circ$, all tilt angles, and $\beta = 0^\circ$ is shown in Figure 11.a, while the roll moment variation with respect to AoA for $\delta_{TW} = 0^\circ$, all aileron deflections and $\beta = -15^\circ$ is shown in Figure 11.b. Except for $\delta_{TW} = 0^\circ$ with respect to AoA, the rolling moment appears to be constant for all tilt angles. Since there is no aileron deflection at $\delta_{TW} = 90^\circ$, the roll moment is measured as zero. At $\delta_{TW} = 90^\circ$, flaps are used instead of ailerons.

Since there is no vertical tail to stabilize the directional axis, the aircraft is directionally unstable. Figure 12.a shows that the yaw moment decreases as the AoA increases for all tilt angles. $\beta = -15^\circ$ and $\delta_a = 20^\circ$ are used in Figure 12.a, while $\delta_{TW} = 0^\circ$ is employed in Figure 12.b. The use of differential thrust front motors will improve directional axis stability.

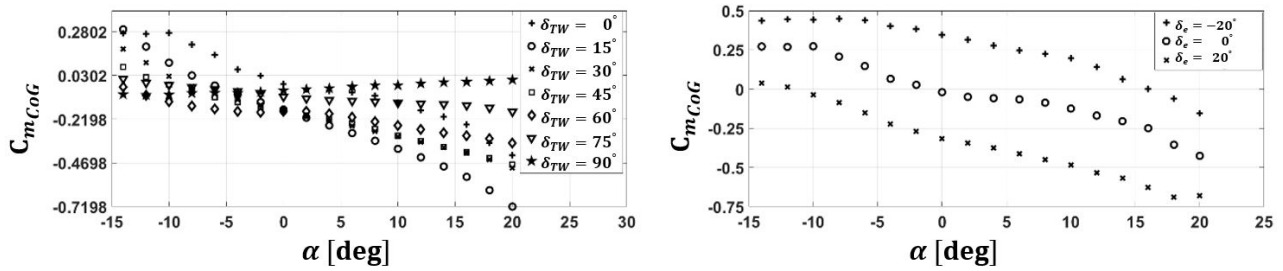


Figure 10. Pitching moment coefficient, C_m , variation with angle of attack for different tilt-wing angles.

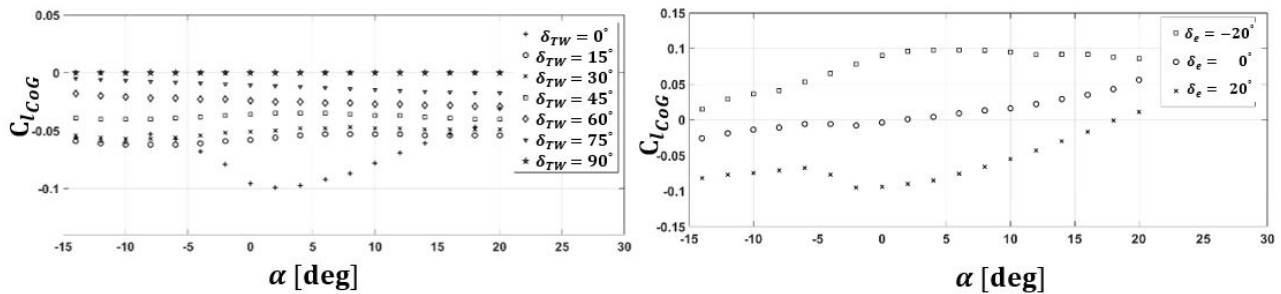


Figure 11. Rolling moment coefficient, C_l , variation with angle of attack for different tilt-wing angles.

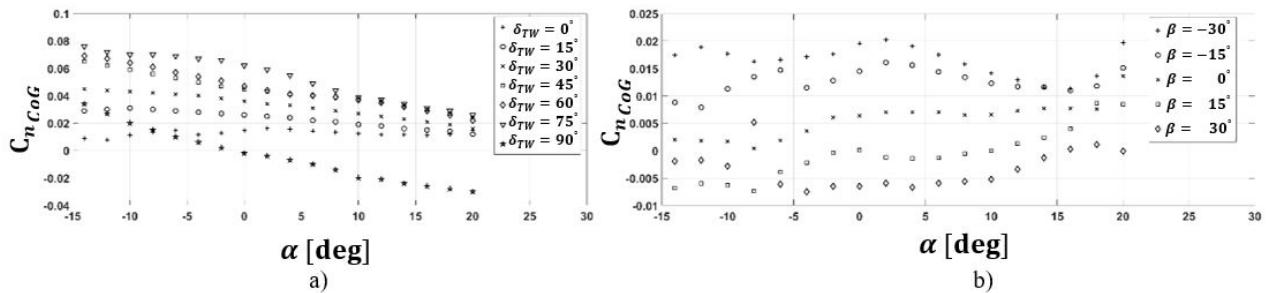


Figure 12. Yawing moment coefficient, C_n , variation with angle of attack for different tilt-wing angles.

Using Fluent and CFD Post Features, the pressure coefficient and vorticity contours were obtained. In fluid dynamics, the pressure coefficient is a dimensionless number that defines relative pressures across a flow field. TWA, aileron, elevator deflections, angle of attack, and sideslip angles are all zero in the baseline flight state (Figure 13) . With the use of pressure and vorticity contours, each flight state is compared to the baseline scenario. All figures between Figure 13 and 23 are gathered from the CFD Post Process tool.

Pressure on the bottom of the wing increases as the angle of attack increases, as seen in Figure 14. Figure 8 shows how this condition raises C_L coefficient. We may also deduce from pressure distribution in Figure 14 that the pressure center moves forward, causing C_m to decrease.

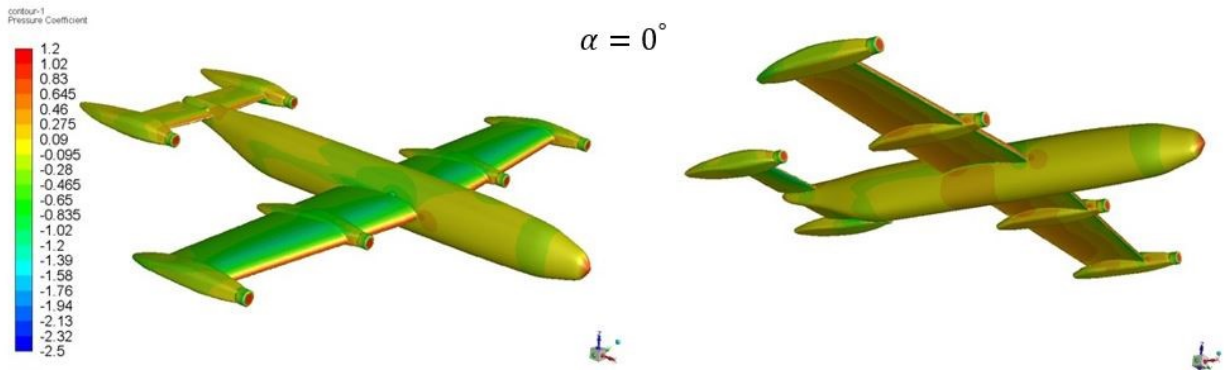


Figure 13. Pressure contours at baseline flight state ($\alpha=0^\circ$)

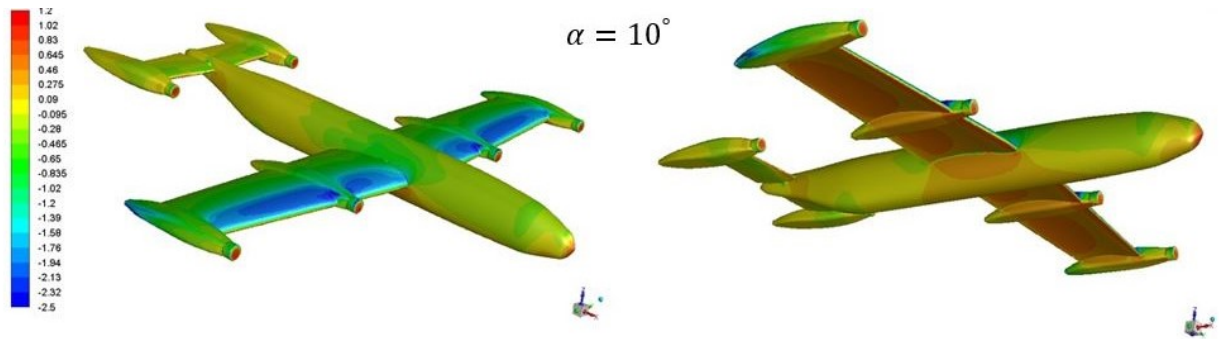


Figure 14. Pressure Contours at 10° Angle of Attack

Figure 15 shows the pressure counters at a fifteen-degree side slip angle. Figure 15 indicates that aircraft have an asymmetric pressure distribution, resulting in a decrease in C_n and a rise in C_l coefficients. Furthermore, as can be seen in Figure 15, the pressure coefficient is slightly decreasing as the side-slip increases. C_L decreases as a result of this condition. It's worth noting that the side-slip angle is positive, indicating that airflow is coming from the right side of the aircraft. The stagnation point shifts to the fuselage's right side.

Figure 16 shows that when the elevator is negatively deflected, the static pressure on the upper side of the horizontal stabilizer increases. As can be seen in Figure 10, this condition causes the center of pressure to shift backwards, resulting in a positive moment on the aircraft. C_L is also affected by an increase in pressure on the upper side of the elevator. The overall lift decreases as the pressure on the upper side of the plane rises.

In most parts of the mission, roll moment is obtained by aileron deflection. There is a difference in pressure distribution between aileron deflection and no deflection. The rise in pressure at the bottom of the right-wing is astounding (Figure 17). This pressure differential causes a roll moment and an extra lift on the right side. On roll moment, the left side is also involved, but the right-wing contributes the most.

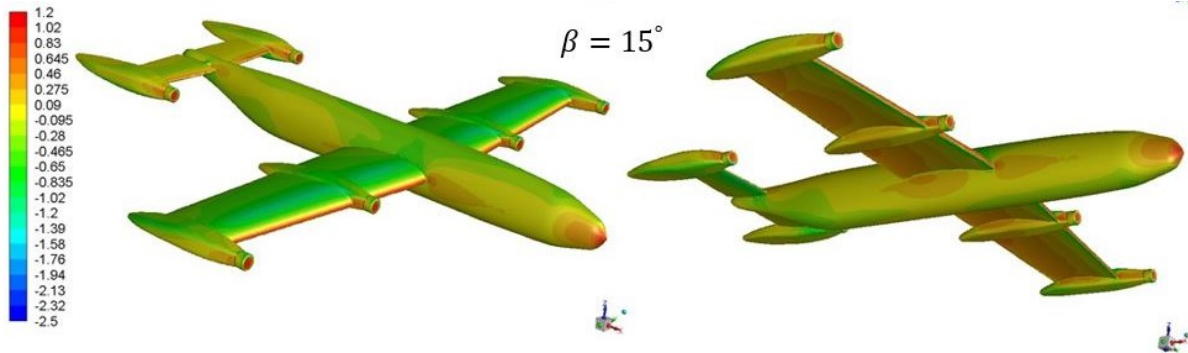


Figure 15. Pressure contours at 15° sideslip angle ($\alpha=0^\circ$).

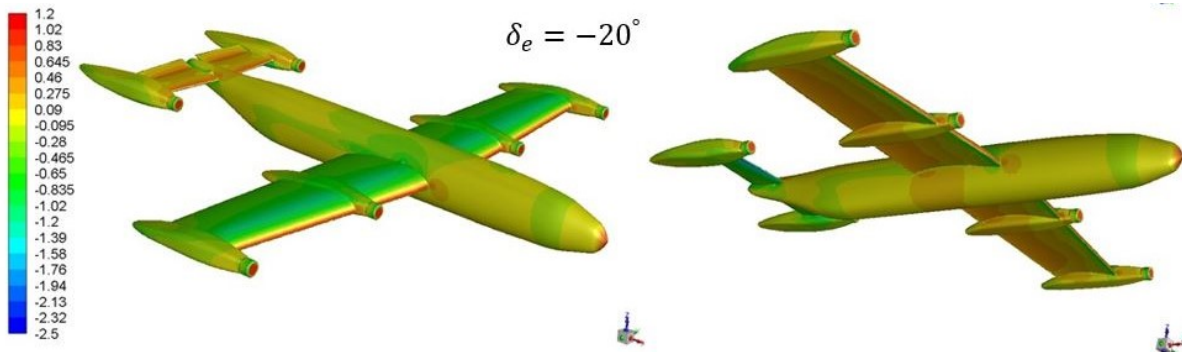


Figure 16. Pressure contours at -20° elevator deflection ($\alpha=0^\circ$).

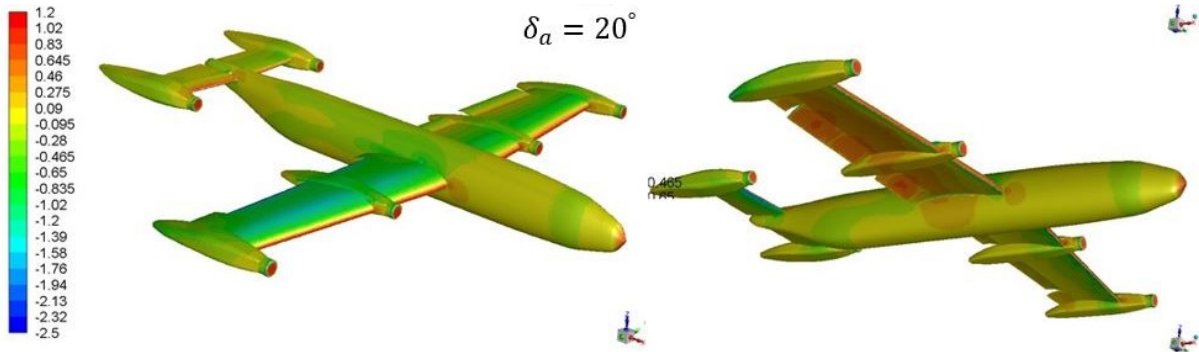


Figure 17. Pressure contours at 20° aileron deflection ($\alpha=0^\circ$).

The effect of Tilt Wing Angle on pressure distribution is shown in Figure 18. Each distribution was calculated at a 0-degree AoA. The fuselage at 45 degrees tilt angle exerts pressure on the wing root. The lift on the wing generates force on the body x-axis at 90 degrees, which is used in longitudinal control. If the tilt angle increases, pressure builds up on the upper side of the fuselage. The aircraft's lift is reduced as a result of this condition.

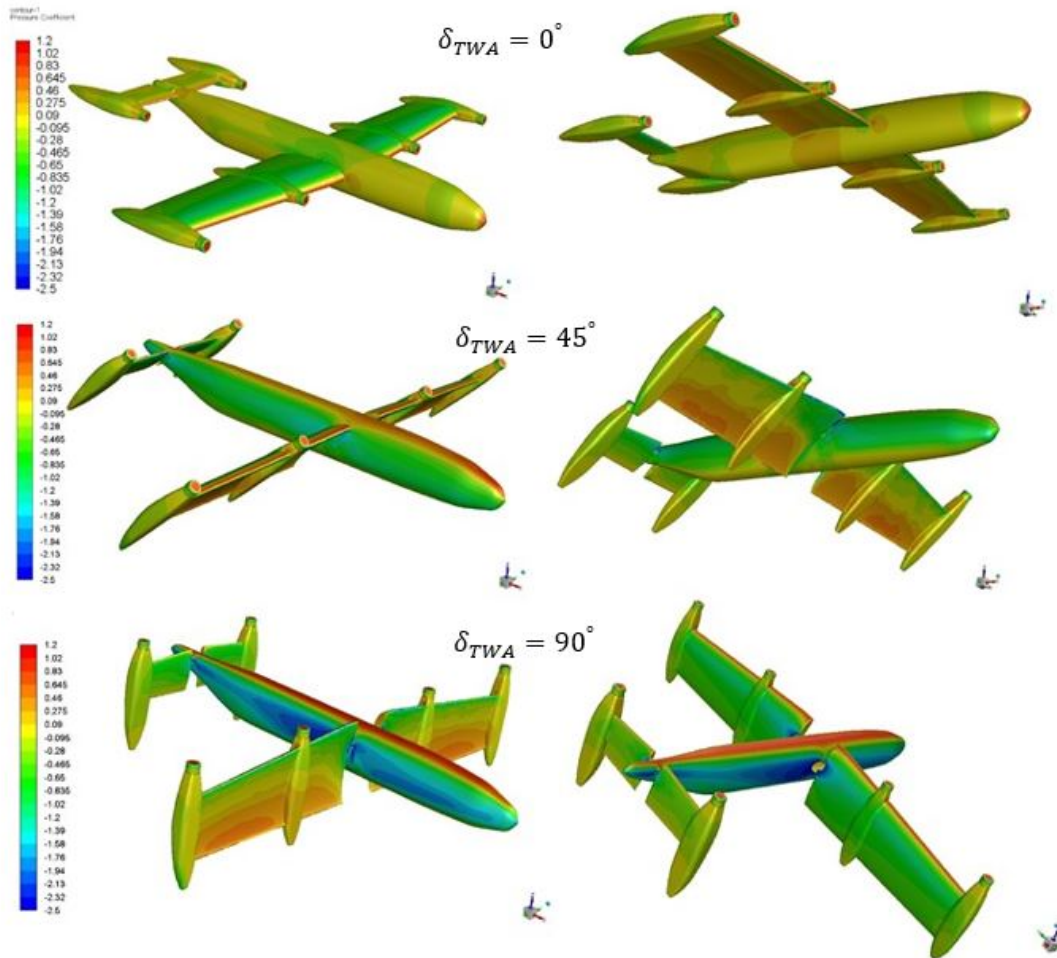


Figure 18. Pressure contours at different tilt angles.

The magnitude of the vorticity increases as the AoA increases, as predicted (Figure 19). Powerful vorticities exist behind the engine nacelles, which could be optimized based on these findings.

As expected, asymmetric vorticity contours emerged in Figure 20. Vorticity rises as the sideslip angle rises. Note that, the vorticity contours were plotted in a plane 10 centimeters away from the wingtip engine nacelles. When the distance between engine nacelles is increased, different vorticity contours can be obtained.

The elevator deflection effect on the vorticity contours is shown in Figure 21. Vorticity contours in two conditions have almost identical trends, with only minor variations. Due to wing and elevator contact, the backside of the root engine nacelles is slightly altered. Vorticity is influenced when the elevator's pressure is increased.

Owing to the affected flow behind the ailerons, aileron deflection produces additional singularities on vorticity contours. Aileron deflection also affects vorticity contours across the fuselage, as shown in Figure 22. It's worth noting that negative aileron deflection produces more vorticity contours than positive aileron deflection, implying that the flow behind the left-wing is more affected than the right wing.

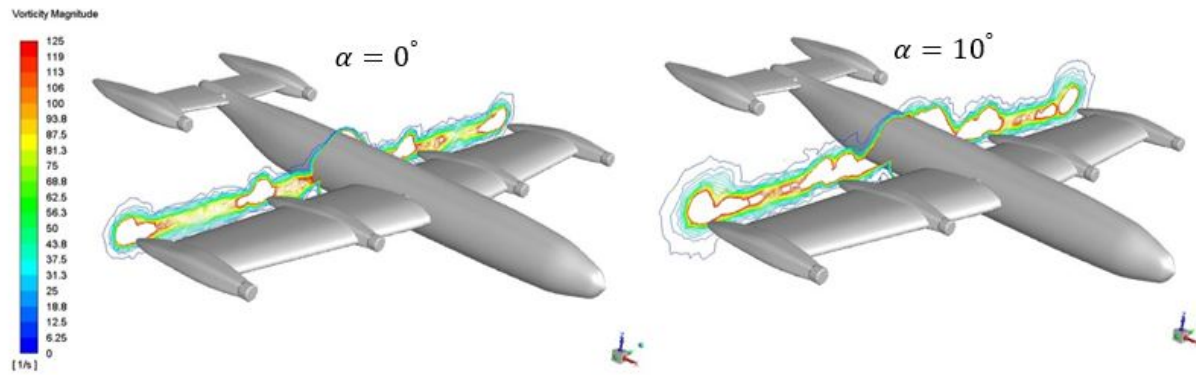


Figure 19. Vorticity contours at different angles of attack.

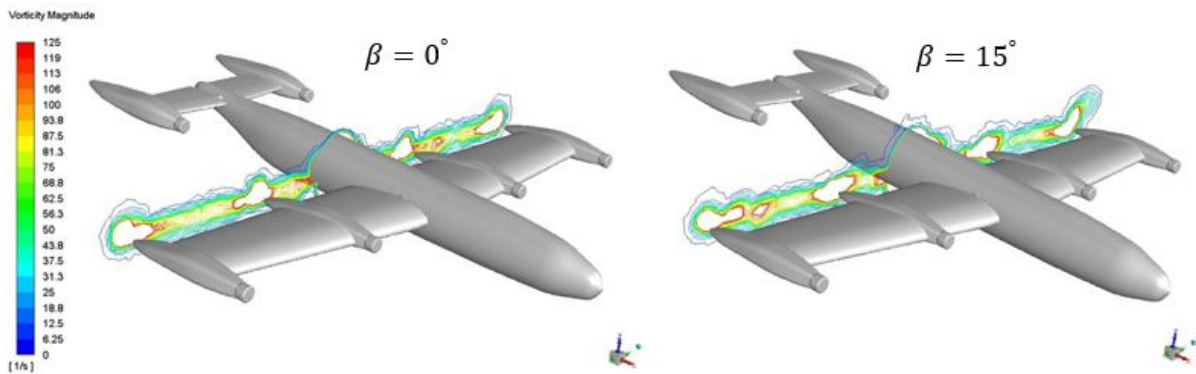


Figure 20. Vorticity contours at different sideslip angles.

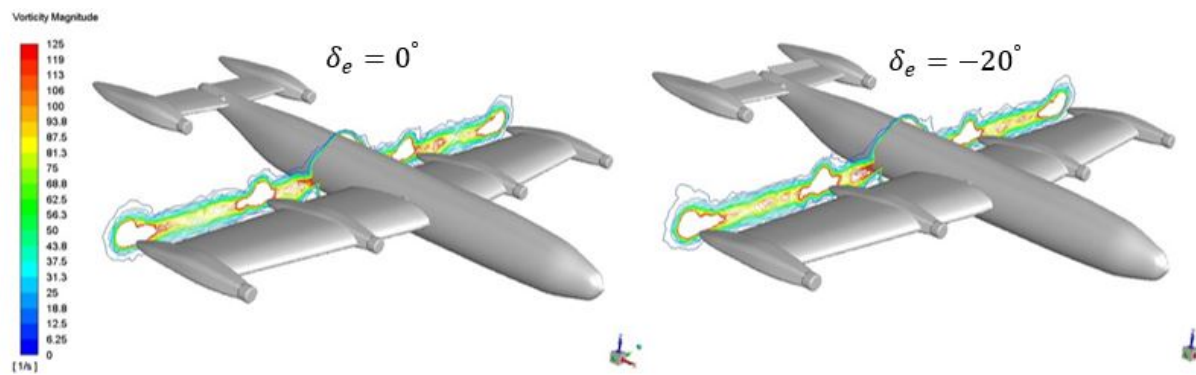


Figure 21. Vorticity contours at different elevator angles.

Tilt wing deflection plays a role in vorticity formation as well (Figure 23). Vorticity increases exponentially as the tilt angle approaches 45 degrees. Tilt angles between 0 and 90 degrees, on the other hand, exhibit identical behaviors.

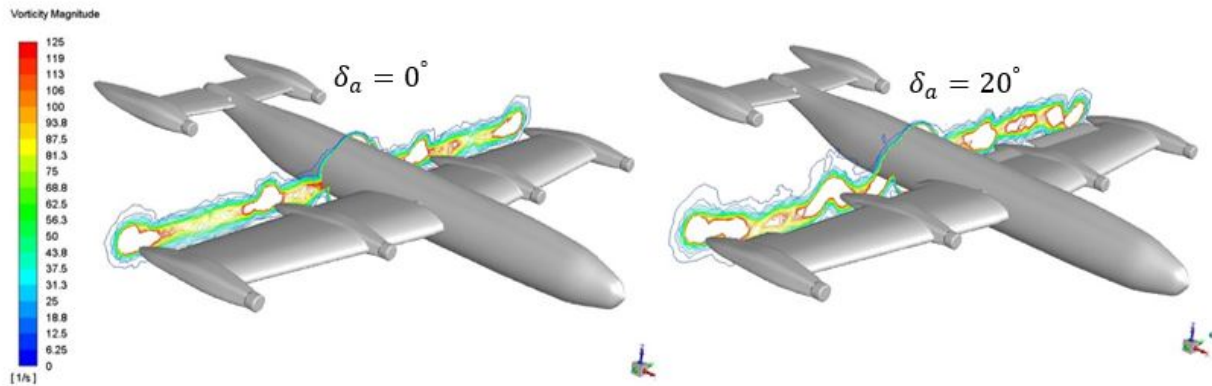


Figure 22. Vorticity contours at different aileron angles.

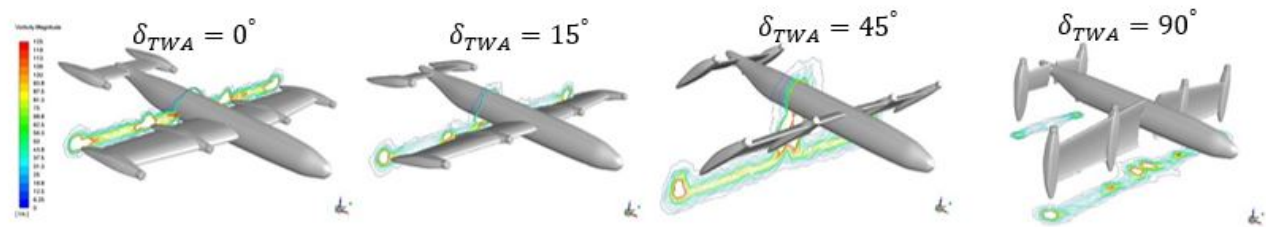


Figure 23. Vorticity contours at different tilt angles.

5. Conclusion

A VTOL UAV was designed and the CFD results were presented. To reduce time delays caused by engine transient output, electrically driven motors are used. To effectively manipulate the slipstream of propellers, the distributed electric propulsion principle was used. The propellers are chosen to be as wide as possible so that they can cover the entire wing. Nonetheless, the distance between two propellers and the distance between propeller and fuselage are limiting factors. The fuselage was designed with the goal of reducing the drag coefficient as much as possible while still allowing enough place for the components. The S1223 airfoil was chosen because it has a low stall speed and a good lift-to-drag ratio. CFD analysis was used to calculate the lift, drag, and moment coefficients. For this analysis, there was no use of a vertical tail. Since the vertical tail was not used as part of this analysis, a 5% weight reduction and a 4% drag reduction were achieved. CFD analysis has shown that the platform has adequate aerodynamic performance. For the transition between flight modes, a CFD database has been developed that can be used in similar studies. The CFD was used to examine seven trim points. The contours of pressure and vorticity have been plotted. These findings will be used to develop the tilt-wing aircraft controller in the future researches.

References

- [1] Kurtulus D.F. Introduction to micro air vehicles: concepts, design and applications. In: Decuyper R, Carbonaro M, editors. Recent developments in unmanned aircraft systems (UAS, including UAV and MAV). Von Karman Institute for Fluid Dynamics; 2011. p. 219–255
- [2] Nonami K, Kendoul F, Suzuki S, Wang W, and Nakazawa D. Autonomous flying robots: Unmanned aerial vehicles and micro aerial vehicles. Springer; 2010th edition; 2010. p. 1-329.
- [3] Cakici F. Control and Guidance of a Multi-Mode Unmanned Aerial Vehicle for Increased Versatility [dissertation]. Electrical and Electronics Engineering: Middle East Technical University; 2016.
- [4] Mcswain R.G, Glaab L.J, Theodore C.R. Greased Lightning (GL-10) Performance Flight Research-Flight Data Report. Virginia: Langley Research Center; 2017. Report No.: NASA/TM-2017-219794
- [5] Muraoka K, Okada N, Kubo D, Daisuk M. Transition flight of quad tilt wing VTOL UAV. Proceedings of the 28th International Congress of The Aeronautical Sciences; 2012 Sep 23-28; Brisbane, Australia.
- [6] Rohde S, Goddemeier N, Wietfeld C, Steinick F, Hinrichs K, Ostermann T et al. AVIGLE: A system of systems concept for an avionic digital service platform based on Micro Unmanned Aerial Vehicles. Proceed-ings of the 2010 IEEE International Conference on Systems, Man and Cybernetics; 2010 Oct 10-13; Istanbul, Turkey.
- [7] Muraoka K, Okada N, Kubo D, editors. Quad Tilt Wing VTOL UAV: Aerodynamic Characteristics and Proto-type Flight. Proceedings of the AIAA InfoTech Aerospace Conference; 2009 April; Seattle, Washington, USA.
- [8] Lee J, Min B, Kim E. Autopilot design of tilt-rotor UAV using particle swarm optimization method. Proceedings of the Control, Automation and Systems; 2007 November; Seoul, Korea.
- [9] Cetinsoy E, Dikyar S, Hancer C, Oner K, Sirimoglu E, Unel M et al. Design and construction of a novel quad tilt-wing UAV. Mechatronics 2012;22(6):723–745.
- [10] Cetinsoy E, Sirimoglu E, Oner K, Hancer C, Unel M, Aksit M, Kandemir I, Gulez K. Design and Development of a Tilt-Wing UAV. Turkish Journal of Electrical Engineering and Computer Science 2011.
- [11] Onen A.S, Cevher L, Senipek M, Mutlu T, Gungor O, Ozdemir I, et al. Modeling and controller design of a VTOL UAV. Proceedings of the 2015 International Conference on Unmanned Aircraft Systems (ICUAS); 2015 June 09-12; Denver, CO, USA.
- [12] Ozdemir U, Aktas Y.O, Vuruskan A, Dereli Y. “Design of a commercial hybrid VTOL UAV system,” J. Intell. Robot. Syst. Theory Appl., vol. 74, no. 1–2, pp. 371–393, 2014.
- [13] Oktay T, Uzun M, Celik H, Konar M. PID Based Hierarchical Autonomous System Performance Maximization Of A Hybrid Unmanned Aerial Vehicle (HUAV). Anadolu University Journal Of Science And Technology A - Applied Sciences and Engineering, cilt.18, ss.1, 2017.
- [14] Armutcuoglu O, Kavsaoglu M, Tekinalp O. Tilt Duct Vertical Takeoff and Landing Uninhabited Aerial Vehicle Concept Design Study. Journal Of Aircraft, Vol. 41, No. 2, 2004.
- [15] ANSYS v.18, Fluent, ANSYS, Inc., Southpointe, 2600 Ansys Drive, Canonsburg, PA 15317, USA, 2018.
- [16] Raymer D. Aircraft design: A conceptual approach. ARC; 6th edition; 2018. p. 1-800.
- [17] xflr5.tech [Internet]. Open-source software [updated 2020 May 16; cited 2020 Jul 9]. Available from: <http://www.xflr5.tech/xflr5.htm>.
- [18] Nunoa S.I.I.U. 2010 Design Build and Fly Competition Top Scored Reports. AIAA; 2010. vol. 60, no. 4, pp. 982–992.
- [19] Rothhaar P.M. NASA Langley distributed propulsion VTOL tilt-wing aircraft testing, modeling, simulation, control, and flight test development. Virginia: Langley Research Center; 2014. Report No.: AI-AA-2014-2999.
- [20] ecalc.ch [Internet]. Open-source software [updated 2020 May 16; cited 2020 Jul 9]. Available from: <https://ecalc.ch/setupfinder.php?neumotors>.

- [21] Selig M.S. "AIAA Atmospheric Flight Mechanics 2010 Conference Modeling Propeller Aerodynamics and Slipstream Effects on Small UAVs in Realtime," AIAA Atmos. Flight Mech. 2010 Conf., pp. 1-23, 2010.
- [22] Cetinsoy E, Hancer C, Oner K, Sirimoglu E, Unel M. Aerodynamic design and characterization of a quad tilt-wing UAV via wind tunnel tests. *Journal of Aerospace Engineering* 2012; 25(4):574-587.